

## Fabrication of Nanoporous Ni by Chemical Dealloying Al from Ni-Al Alloys for Lithium-ion Batteries

Md. Arafat Rahman<sup>1</sup>, Xinkun Zhu<sup>2</sup>, and Cuie Wen<sup>1,3,\*</sup>

<sup>1</sup>Faculty of Science, Engineering and Technology, Swinburne University of Technology, Hawthorn, Victoria 3122, Australia

<sup>2</sup>Faculty of Material Science and Engineering, Kunming University of Science and Technology, Kunming, Yunnan 650093, China

<sup>3</sup>School of Aerospace, Mechanical and Manufacturing Engineering, RMIT University, Bundoora, Victoria 3083, Australia

\*E-mail: [cuie.wen@rmit.edu.au](mailto:cuie.wen@rmit.edu.au)

Received: 21 January 2015 / Accepted: 3 March 2015 / Published: 23 March 2015

---

Nanoporous nickel (np-Ni) was fabricated through dealloying of Ni-Al alloys and its application in lithium-ion batteries (LIBs) was assessed. The effect of alloy composition of the Ni-Al alloys on the formation of np-Ni has been investigated using X-ray diffraction (XRD), scanning electron microscopy combined with energy dispersive X-ray spectrometry (SEM-EDX), and 3D profilometry analysis. The experimental results show that the Ni-Al alloy composition has a significant effect on the dealloying feasibility, the phase constituents and the microstructures of the resultant np-Ni. As compared to Ni<sub>50</sub>Al<sub>50</sub> alloy, Ni<sub>30</sub>Al<sub>70</sub> was easier for dealloying since the percentage of Ni content is higher in Ni<sub>50</sub>Al<sub>50</sub>. SEM images revealed that the np-Ni exhibited approximately a mean inner diameter of 71.10 ± 43.69 nm and 40.84 ± 24.70 nm for the Ni<sub>30</sub>Al<sub>70</sub> and Ni<sub>50</sub>Al<sub>50</sub> alloy, respectively. Pore distribution analysis revealed that due to the multiple intermetallic phases in the precursor Ni-Al alloys, the nanoporous structure was heterogeneous with a large variation in pore size and porosity. 3D profilometry revealed that almost all of the surfaces of the as-formed np-Ni displayed a leptokurtic distribution. In addition, the surface area, pore volume, and mean pore diameter of the np-Ni were assessed using Brunauer-Emmett-Teller (BET) analysis. The specific surface area of the np-Ni dealloyed from Ni<sub>30</sub>Al<sub>70</sub> alloy was as high as 198.70 m<sup>2</sup> g<sup>-1</sup> compared to 9.46 m<sup>2</sup> g<sup>-1</sup> for dealloyed from Ni<sub>50</sub>Al<sub>50</sub> alloy. The as-dealloyed np-Ni was used as negative electrode of LIBs and the performance was evaluated. The dealloyed np-Ni from Ni<sub>30</sub>Al<sub>70</sub> alloy with an oxide (NiO) layer surface and highly conductive Ni metal cores exhibited maximum discharge capacity of 651 mA h g<sup>-1</sup> at 1C rate after 9<sup>th</sup> cycle, which is reduced to a neglectable level of 80 mA h g<sup>-1</sup> after 150<sup>th</sup> cycles.

---

**Keywords:** Nanoporous-nickel (np-Ni), Dealloying, Pore distribution, Capacity.

## 1. INTRODUCTION

Nanoporous materials have been studied for a variety of applications, for example gas sensors [1], catalysts [2], and structural materials [3]. It has been reported that nanoporous metals can be self-assembled by dealloying or selective dissolution of a less noble component from a binary alloy [4]. Nanoporous metals with highly ordered networks and narrow pore-size distributions are of particular interest for a wide range of important potential applications, for example electrochemical catalysis for its high active surface area and improved electron mobility in the solid ligament [5, 6]. However, the synthesis of nanoporous metals faces great challenges, since metals at the nanoscale favor low surface areas in order to minimize the surface energy.

Noble metals such as palladium, platinum, and gold as nanoclusters can be incorporated into the nanoporous domains for catalysis applications [7-9]. Nanoporous gold represents the prototypical example of nanoporous metals which can be conferred a nanoporous structure by dealloying. The np-Ni is a potentially low-cost alternative to precious-metal catalysts [10]. The benefit of employing np-Ni is taking the advantage of its electronic band structure that promotes the reaction of interests and a high specific surface area to reagent contact. The high surface area of porous metals allows the electrolyte access, resulting in fast charge/discharge characteristics. Nickel is typically used as the negative electrode, being one of the few materials that can withstand the repeated cycling and the associated volumetric changes. Nickel foam with a nanoporous structure can be obtained by several methods such as alkaline leaching aluminium (Al) from Ni-Al Raney nickel [11], chemical vapour deposition (CVD) [12, 13], electrodeposition [14], powder metallurgy [15] and so on. However, these processes were found to be imperfect due to limitations in controlling pore sizes and relative density which are important for metallic foams. Chemical dealloying has been selected for the fabrication process for np-Ni from Ni-Al alloys in this study due to a number of merits such as easy handling and simple instrumental setup. The resultant np-Ni with a naturally formed oxide surface was used as binder-free electrode for LIBs and its performance was evaluated.

## 2. MECHANISM OF DEALLOYING

Dealloying can be interpreted as a reaction-diffusion process, where the less noble metal in a solid solution is dissolved at the solid/liquid interface to an acid or alkaline solution, leaving behind a porous structure. The reason for the dissolution of the less noble metal dissolution has been reported to be the thermodynamics of the alloy/electrolyte interface [4, 16]. Fig. 1 shows the schematic illustration of how porosity evolves during selective dissolution of Al from  $\text{Ni}_x\text{-Al}_{1-x}$  alloys. At the first step, the surface of the Ni-Al alloys is exposed with regions of accumulated noble component (Ni) at the base of the already-formed nanoporous skeleton. Atoms of the less noble component (Al) in the exposed alloy surface are dissolved into the electrolyte. In the second stage, the surface area increases with increasing interfaces during dissolving in first step and the noble Ni atoms are released onto the surface. These Ni atoms are condensed onto already-agglomerated Ni atom clusters, or nucleate new clusters when

Ni atom ligaments are too far away. In the final stage, the less noble element (Al) in the Ni-Al alloy surface dissolves into the electrolyte; Ni agglomeration repeats and pore surface area increases.

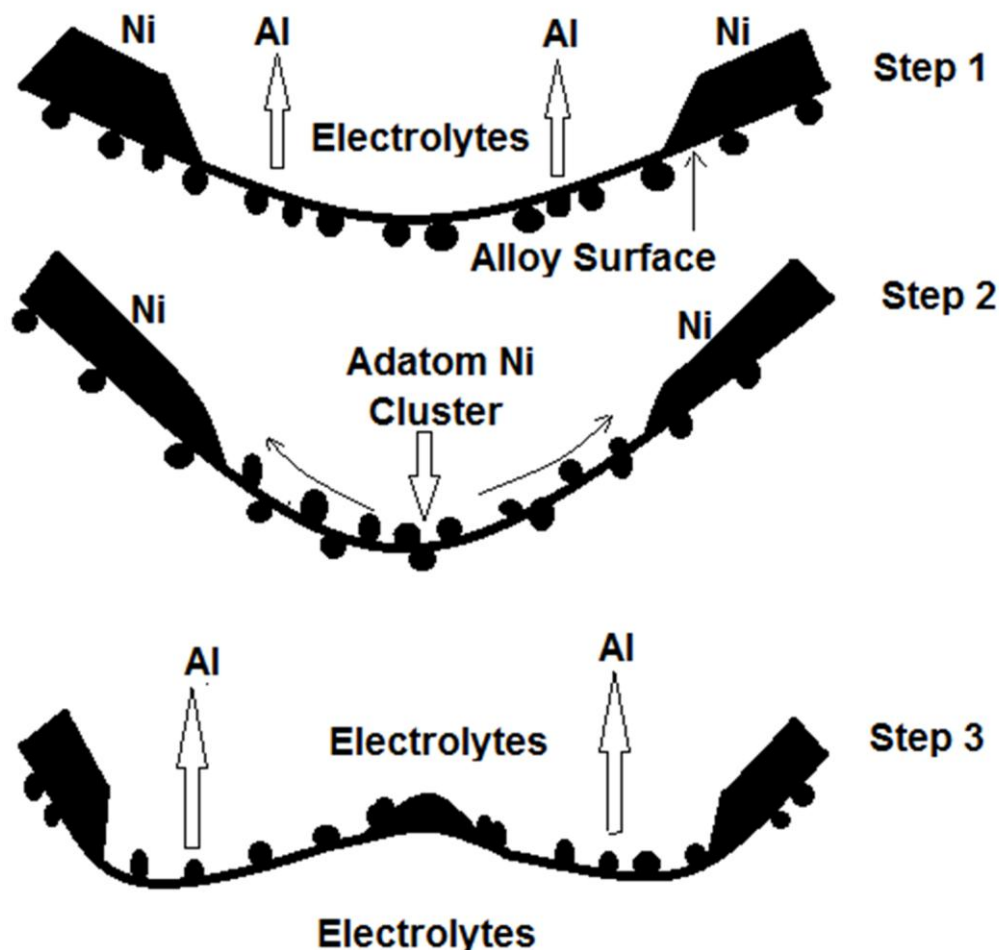
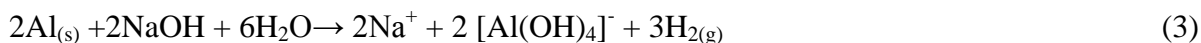


**Figure 1.** Schematic illustration of porosity evolution during chemical dealloying of Al from Ni<sub>x</sub>Al<sub>1-x</sub> alloys

In this study, Ni-Al alloys have been used as the precursor materials. Aluminum does not react with water under normal circumstances, as an impermeable protective layer composed of aluminum hydroxide either forms within a second or is already in place. The formation of the protective layer is prevented with the addition of sodium hydroxide. With the production of aluminates (Al(OH)<sub>4</sub><sup>-</sup>), the amphoteric (capable of acting as either an acid or a base) aluminum hydroxide (Al(OH)<sub>3</sub>) goes in solution as follows:



During these reactions, Al atoms in the Ni-Al intermetallic compounds are continuously dissolved into the solution and hydrogen (H<sub>2</sub>) bubbles come out of the sample surface. The bubbles

emerge rapidly at the beginning of the dealloying, and disappear slowly as dealloying is processed. The dealloying rate gradually decreases. The reactions practically stop when Al is dissolved in the NaOH solution. The Ni atoms remain stable during chemical dealloying because Ni does not react with NaOH.

### 3. EXPERIMENTAL METHOD

Ni-Al alloy ingots having compositions of Ni<sub>30</sub>Al<sub>70</sub>, and Ni<sub>50</sub>Al<sub>50</sub> (at% hereafter) were used as precursor materials. The fabrication procedure of np-Ni by dealloying is illustrated in Fig. 2. Pure Ni (purity 99.95%) and pure Al (purity 99.99% ) slices were used as starting materials for casting the Ni-Al alloys. The Ni and Al were weighed in atomic ratios of the nominal compositions and mixed together. The mixed Ni and Al slices were placed in a graphite die (outside diameter, 30 mm; inside diameter, 20 mm; height, 40 mm) and then introduced into a high frequency induction furnace, which consist of a quartz tube and an inductive heating cylinder of graphite. Before heating, the chamber was flushed with high-purity argon (Ar) gas to eliminate oxygen (O<sub>2</sub>) by means of a rotary vacuum pump for three times. Subsequently, the furnace was rapidly heated up from room temperature to around 1455 °C within 2 min and maintained for the Ni and Al to react for 5 min under a total pressure of 50–100 Torr. When the Ni-Al alloy was melted homogenously, the furnace was cooled down by furnace cooling to room temperature and Ni-Al alloy ingots were obtained for further dealloying experiments. Nanoporous Ni (np-Ni) were fabricated by chemical dealloying in 1 M NaOH at room temperature. After dealloying, the samples were rinsed thoroughly with deionized water and ethanol.

Anodic polarization measurement on the Ni-Al alloys was conducted in 1 M NaOH to analyze the dissolving behavior of Al during chemical dealloying. A three-electrode electrochemical cell with a Pt plate electrode (1 cm<sup>2</sup>) as a counter electrode, a saturated calomel electrode (SCE) as a reference electrode, and the alloy disc as a working electrode was used. The alloy surface of 1.0 cm<sup>2</sup> was exposed in 50 ml of 1 M NaOH solution during anodic polarization test.

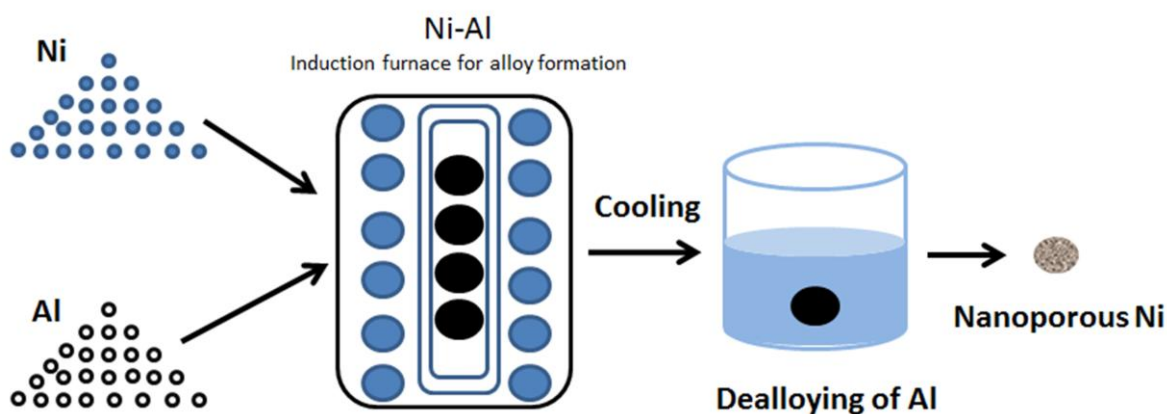


**Figure 2.** Schematic illustration of fabrication of nanoporous Ni by dealloying

The current-potential behavior data was collected by using a PARSTAT<sup>®</sup> 2273 electrochemical station combined with PowerCORR software. Starting from the open-circuit potential, the potential was positively scanned to 1.7 V (since Ni/Ni<sup>2+</sup> -0.23V vs. SCE and Al/Al<sup>3+</sup> -1.66 V vs. SCE) at a scan rate of 1 mV s<sup>-1</sup> for all anodic polarization measurement.

The surface roughness of the as-dealloyed Ni-Al alloys has been measured by using a 3D profilometer (ContourGT-K, Bruker Nano, USA). The morphologies and chemical compositions of the samples were examined using a scanning electron microscope combined with energy-dispersive X-ray spectrometer (SEM-EDXSUPRA 40 VP, Zeiss). The phases of the Ni-Al alloy samples before and after dealloying were analyzed by using X-ray diffractometry with Cu K $\alpha$  as the radiation source. The diffraction patterns were recorded over 2 $\theta$  ranging from 10 to 90 $^{\circ}$  at a step size of 0.02 $^{\circ}$ . Nitrogen gas (N<sub>2</sub>) adsorption isotherms and Brunauer-Emmett-Teller (BET) surface area analysis data were collected using a BELSORP-max instrument (BEL Inc. Japan).

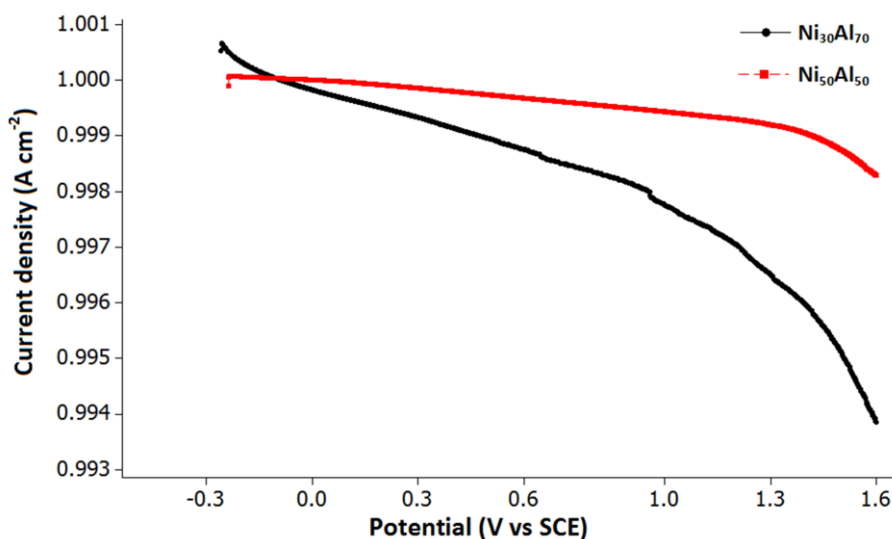
The np-Ni fabricated from dealloying of Ni-Al alloys was used as the negative electrode of LIBs. The positive electrode was metallic lithium foil with a surface area about 2.0 cm<sup>2</sup> and 0.01 cm thick. CR2032-type coin cells were assembled in an argon gas filled glove box with O<sub>2</sub> content below 0.1 %. The electrolyte used for the LIBs was 1.0 M LiPF<sub>6</sub> (Sigma-Aldrich). Celgard 2400 polyethylene was used as the separator. The separator, current collector, battery casings, and spacer were dried at 60  $^{\circ}$ C under vacuum over 24 h. Data acquisition and analysis were performed using the battery testing instruments LANHE-CT2001A and LANDt, respectively. Cyclic voltametric (CV) and electrochemical impedance spectroscopy (EIS) was performed with a PARSTAT<sup>®</sup> 2273 electrochemical station. Electrochemical software PowerSine and PowerCV were employed for impedance and CV data acquisition, respectively. The amplitude for EIS measurement was 10 mV, the range of the frequency was from 100 kHz to 10.0 mHz. The CV measurements were performed at scan rate of 0.1 mV s<sup>-1</sup> in the range of 4.2 V to 0.02 V. All measurements were conducted at room temperature.

## 4. RESULTS AND DISCUSSION

### 4.1 Structural and morphological characterization

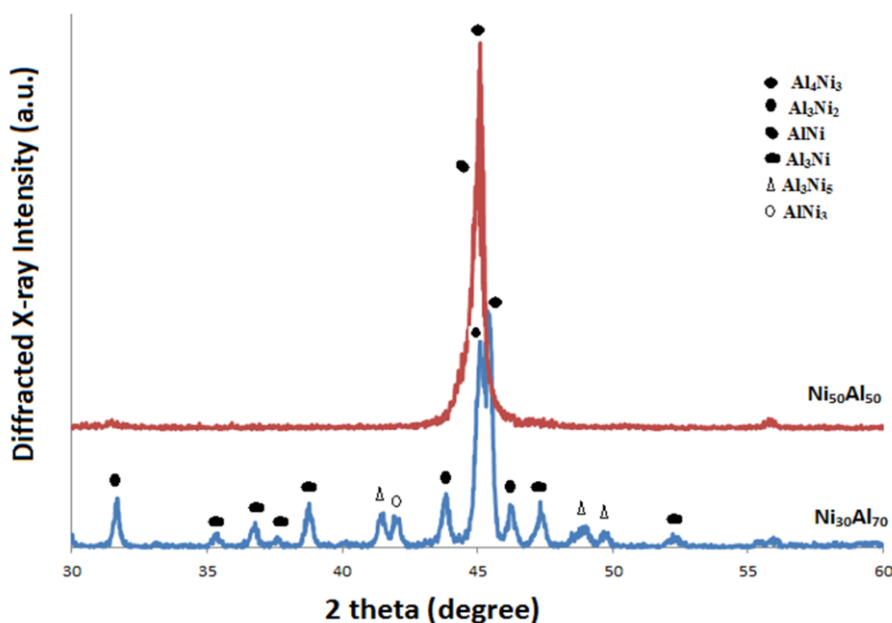
The anodic polarization curves for the precursor materials, Ni<sub>30</sub>Al<sub>70</sub> and Ni<sub>50</sub>Al<sub>50</sub> alloys are shown in Fig. 3. The vertical axis in Fig. 3 shows the apparent current density calculated by simply dividing the measured current by the apparent exposed area of 1.0 cm<sup>2</sup>, although the true surface area is slightly different due to the rough surface. The open-circuit potentials for the two alloys were -0.25 V vs. SCE. This fact suggests the Al/Al<sup>2+</sup> or Al/Al<sup>3+</sup> equilibriums in 1 M NaOH electrolyte and hardly affected by the alloyed element Ni. The apparent current monotonically decreased with the applied potential in case of Ni<sub>30</sub>Al<sub>70</sub> alloy, and the apparent current of Ni<sub>50</sub>Al<sub>50</sub> is almost steady over the applied potential (open circuit voltage to 1.6 V) in the electrolyte for the fabrication of np-Ni. The rate of decreasing apparent current density of Ni<sub>30</sub>Al<sub>70</sub> was larger than that of Ni<sub>50</sub>Al<sub>50</sub> since the content of Al in the anode active material was high. It can be concluded that the Ni<sub>30</sub>Al<sub>70</sub> alloy is more

dealloyable than Ni<sub>50</sub>Al<sub>50</sub> alloy; and the common dealloying mechanism as described above is operative in these alloys.



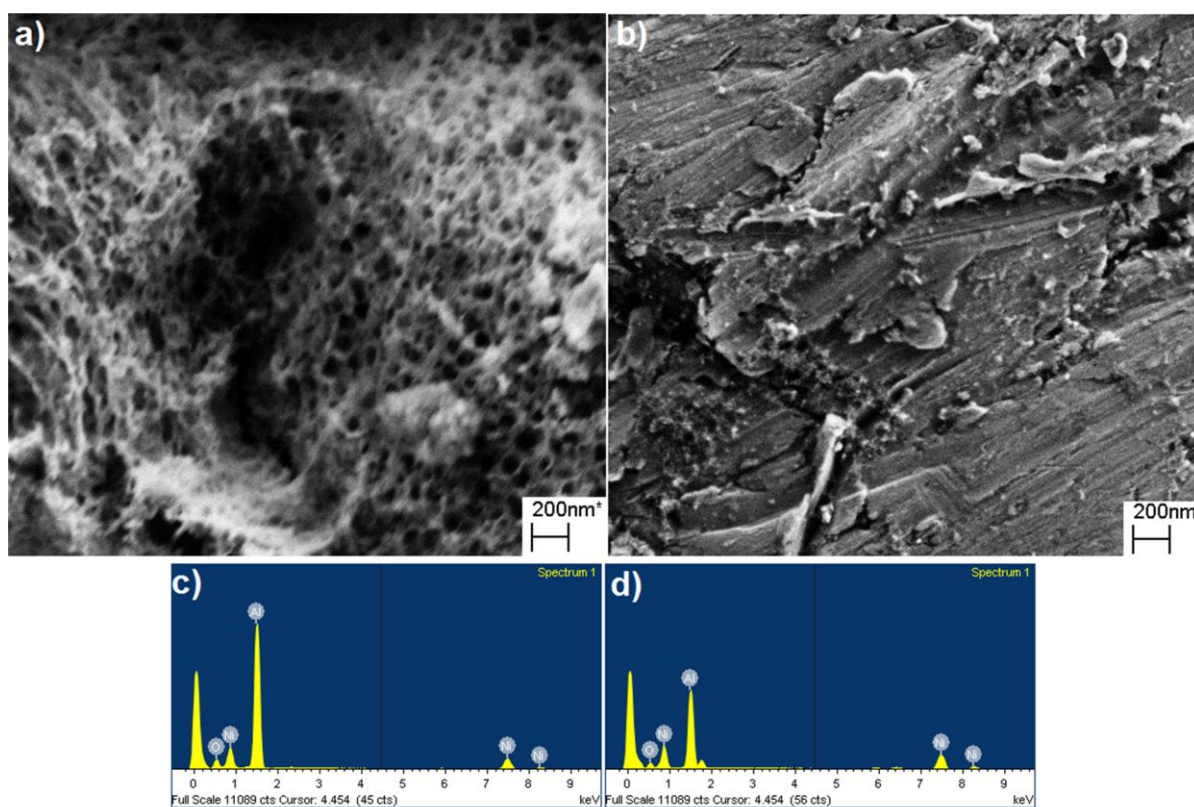
**Figure 3.** Anodic polarization curves for Ni<sub>30</sub>Al<sub>70</sub> and Ni<sub>50</sub>Al<sub>50</sub> before dealloying in 1 M NaOH solution.

Fig. 4 shows the X-ray diffraction patterns of Ni<sub>30</sub>Al<sub>70</sub> and Ni<sub>50</sub>Al<sub>50</sub> alloys. The Ni<sub>30</sub>Al<sub>70</sub> alloy consisted of Al<sub>4</sub>Ni<sub>3</sub>, AlNi<sub>3</sub>, Al<sub>3</sub>Ni<sub>5</sub>, Al<sub>3</sub>Ni<sub>2</sub>, and Al<sub>3</sub>Ni; while Ni<sub>50</sub>Al<sub>50</sub> alloy consisted of Al<sub>4</sub>Ni<sub>3</sub> and AlNi. It is interesting that only one common phase of Al<sub>4</sub>Ni<sub>3</sub> presented in Ni<sub>30</sub>Al<sub>70</sub> and Ni<sub>50</sub>Al<sub>50</sub> alloys.



**Figure 4.** X-ray diffraction patterns of Ni<sub>30</sub>Al<sub>70</sub> and Ni<sub>50</sub>Al<sub>50</sub> before dealloying.

According to the Al-Ni binary phase diagram [17], the phase constituents in equilibrium are  $\text{NiAl}_2 + \text{NiAl}_3$  and solid solution of Ni in NiAl for the  $\text{Ni}_{30}\text{Al}_{70}$ , and  $\text{Ni}_{50}\text{Al}_{50}$  alloys, respectively. It is obvious that the phase constituents of the Ni-Al alloys obtained from furnace cooling deviated from those shown by equilibrium phase diagram since the melting and solidification processes are different. In addition, with increasing Ni contents in  $\text{Ni}_{50}\text{Al}_{50}$  alloy, the number of phase constituents reduced to only two ( $\text{Al}_4\text{Ni}_3$  and AlNi). The phase constituents in the Ni-Al alloys have a significant influence on the dealloying process and formation of np-Ni, since it has been reported that dealloying Al from AlNi phase is difficult [18].



**Figure 5.** SEM images and EDX profiles for np-Ni dealloyed from Ni-Al alloys in 1 M NaOH solution at room temperature: (a, c)  $\text{Ni}_{30}\text{Al}_{70}$ , and (b, d)  $\text{Ni}_{50}\text{Al}_{50}$ .

Fig. 5 shows the microstructures of np-Ni prepared by the dealloying Al from  $\text{Ni}_{30}\text{Al}_{70}$  and  $\text{Ni}_{50}\text{Al}_{50}$  alloys in 1 M NaOH at room temperature. The np-Ni prepared from  $\text{Ni}_{30}\text{Al}_{70}$  alloy exhibited a nanoporous structure throughout the samples (Fig. 5(a)). It is interesting that the morphologies of the np-Ni dealloyed from  $\text{Ni}_{30}\text{Al}_{70}$  alloy were inhomogeneous. In contrast, there were only a few pores with nanoscale pore sizes formed in the  $\text{Ni}_{50}\text{Al}_{50}$  alloy after dealloying (Fig. 5(b)). Qi et al. reported similar results in a study of porous Ni fabricated from rapid solidification and dealloying of  $\text{Al}_x\text{-Ni}$  alloys ( $x = 20, 25, 31.5$  at%) [18]. Their results have shown that the porosity of the porous Ni catalysts decreases with increasing Ni concentrations in the Al-Ni alloys. Also, SEM observations revealed that the pore size of the np-Ni prepared from dealloying of  $\text{Ni}_{50}\text{Al}_{50}$  alloy was smaller than that of  $\text{Ni}_{30}\text{Al}_{70}$

alloy. In addition, complete dealloying of Al from Ni-Al alloy was not possible in this study. There was residue Al presenting in the np-Ni samples after dealloying of Ni<sub>30</sub>Al<sub>70</sub> and Al<sub>50</sub>Al<sub>50</sub> alloys in 1 M NaOH at room temperature according to the EDX results shown in Fig. 5(c) and Fig. 5(d), respectively.

Fig. 6 shows the frequency distribution of the inner pore diameter ( $D_i$ ) of np-Ni after dealloying in 1 M NaOH at room temperature. The graphs of the pore size distribution were generated from 460, and 120 individual measurements from SEM images of the np-Ni dealloyed from Ni<sub>30</sub>Al<sub>70</sub>, and Ni<sub>50</sub>Al<sub>50</sub> alloys, respectively. It was not possible to use the same measurements for pore distribution analysis due to the less number of pores exhibited in the np-Ni dealloyed from Ni<sub>50</sub>Al<sub>50</sub> alloy. The mean inner diameter was  $71.10 \pm 43.69$  nm, and  $40.84 \pm 24.70$  nm of Ni<sub>30</sub>Al<sub>70</sub>, and Ni<sub>50</sub>Al<sub>50</sub> alloy, respectively. It is anticipated that due to the multiple intermetallic phases in the precursor Ni-Al alloys, the porous structure was heterogeneous with a large variation in pore size and porosity. It is observed that  $D_i$  decreased with an increase in the Ni content in the Ni-Al alloys.

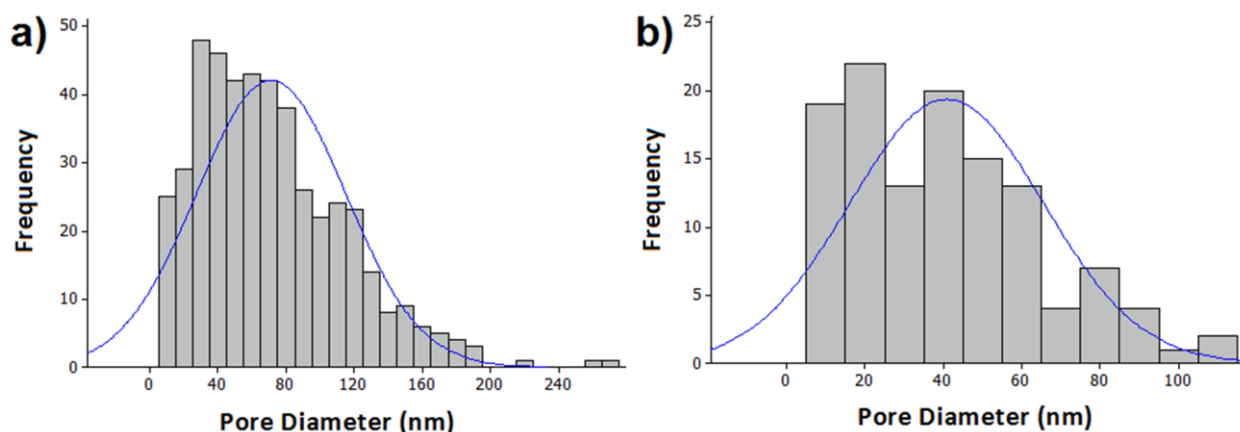


**Figure 6.** Frequency distribution of pore sizes of np-Ni dealloyed at room temperature in 1 M NaOH solution: a) Ni<sub>30</sub>Al<sub>70</sub>, and b) Ni<sub>50</sub>Al<sub>50</sub>.

However, the percentage of pores of the np-Ni dealloyed from Ni<sub>30</sub>Al<sub>70</sub> with  $D_i < 50$  nm is higher than that of the np-Ni dealloyed from Ni<sub>50</sub>Al<sub>50</sub>. One possible reason of less number of pores in the np-Ni dealloyed from Ni<sub>50</sub>Al<sub>50</sub> is that Ni<sub>50</sub>Al<sub>50</sub> contains higher percentage of the nobler species of Ni than Ni<sub>30</sub>Al<sub>70</sub>. Erlebacher et al. [4] and Sieradzki et al. [19] observed the same phenomenon in their studies and concluded that if the nobler metal constituent is of sufficiently high concentration, no selective dissolution can occur.

During dealloying, one or more of the less noble constituents of an alloy system is dissolved from the alloy and the final product is typically composed almost entirely of the more noble metal constituents. The resultant structure consists of open-cellular porous materials in which connecting ligaments and the cells have dimensions of the order of tens on nanometers [4]. The XRD profiles of the np-Ni fabricated by chemical dealloying of Al from Ni<sub>30</sub>Al<sub>70</sub> and Ni<sub>50</sub>Al<sub>50</sub> alloys at room temperature are shown in Fig. 7.

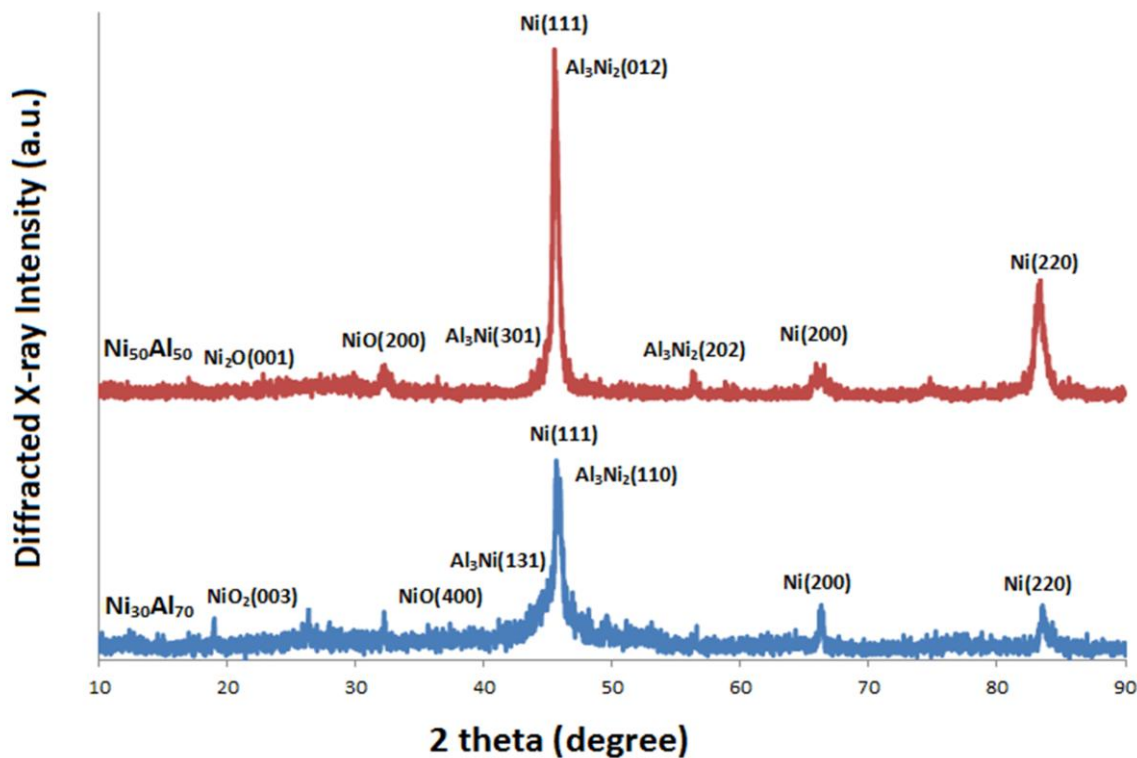


**Figure 7.** XRD patterns of  $\text{Ni}_{30}\text{Al}_{70}$  and  $\text{Ni}_{50}\text{Al}_{50}$  after dealloying at room temperature in 1 M NaOH solution.

The diffraction peaks of the  $\text{Al}_4\text{Ni}_3$ ,  $\text{AlNi}_3$ , and  $\text{Al}_3\text{Ni}_5$  phases disappear on the XRD patterns of the as-dealloyed  $\text{Ni}_{30}\text{Al}_{70}$  samples. However, traces of  $\text{Al}_3\text{Ni}$  and  $\text{Al}_3\text{Ni}_2$  phases are still visible with the peaks of metallic Ni (111), (200), and (222) planes. Similarly, the diffraction peaks of the  $\text{Al}_4\text{Ni}_3$  and  $\text{AlNi}$  phases disappear on the XRD patterns of the as-dealloyed  $\text{Ni}_{50}\text{Al}_{50}$  and the  $\text{Al}_3\text{Ni}$  and  $\text{Al}_3\text{Ni}_2$  phases are still visible. In addition, NiO and  $\text{Ni}_2\text{O}$  phases are detected on the XRD patterns of np-Ni prepared by dealloying  $\text{Ni}_{30}\text{Al}_{70}$  and  $\text{Ni}_{50}\text{Al}_{50}$  alloys (Fig. 7). The existences of NiO and  $\text{Ni}_2\text{O}$  may be attributable to the oxidation of np-Ni due to its high affinity with  $\text{O}_2$ . It should be noted that the residual  $\text{Al}_3\text{Ni}_2$  and  $\text{Al}_3\text{Ni}$  phases were more difficult to be dealloyed than the other phases of  $\text{Al}_4\text{Ni}_3$  and  $\text{AlNi}$  in the Ni-Al alloys. It has been reported that the  $\text{Al}_3\text{Ni}_2$  and  $\text{Al}_3\text{Ni}$  phases are less reactive in alkali solution [20, 21]. In addition,  $\text{Al}_3\text{Ni}_2$  is less vulnerable to alkali attack, as metastable phases are generally considered to have superior corrosion resistance [22]. The noble Ni atoms might arrange themselves on the surface of the Ni-Al alloys to form a dense monolayer, protecting alloys from further dissolution by passivation process [4]. According to the X-ray profile broadening of  $\text{Ni}_{30}\text{Al}_{70}$  and  $\text{Ni}_{50}\text{Al}_{50}$  alloys in Fig. 7, the mean crystal size of the porous Ni can be evaluated by using Scherrer equation. For the  $\text{Ni}_{30}\text{Al}_{70}$  alloy, the mean crystal size of Ni(111), Ni(200), and Ni(220) was calculated to be 73.80 nm, 470.30 nm, and 1684.10 nm, respectively. In contrast, for the  $\text{Ni}_{50}\text{Al}_{50}$  alloy, the mean crystal size of Ni(111), Ni(200), and Ni(220) was calculated to be 18.80 nm, 161.10 nm, and 14.22 nm, respectively. Presumably, between the larger structural units exist larger voids; consequently, the sample with larger crystallites has a smaller surface area.

N<sub>2</sub> adsorption isotherms for the np-Ni fabricated by dealloying of Ni<sub>30</sub>Al<sub>70</sub> and Ni<sub>50</sub>Al<sub>50</sub> for potential catalyst applications are shown in Fig. 8. It is noted that the hysteresis loops of nanoporous Ni from as-dealloyed Ni<sub>30</sub>Al<sub>70</sub> alloy is clearer than that of Ni<sub>50</sub>Al<sub>50</sub> alloy. The isotherms of nanoporous Ni from as-dealloyed Ni<sub>30</sub>Al<sub>70</sub> alloy reveal the stepwise adsorption and desorption branch of type IV curves, indicating the presence of mesoporous/macropores material having a three dimensional (3D) intersection according to the international union of pure and applied chemistry (IUPAC) classification [23, 24]. The hysteresis loop of nanoporous Ni from Ni<sub>30</sub>Al<sub>70</sub> alloy is H3 type according to the IUPAC classification of hysteresis loop. It is believed that this type of isotherm occurs from slit-shaped pores [23]. In contrast, the isotherms of nanoporous Ni from as-dealloyed Ni<sub>50</sub>Al<sub>50</sub> alloy follows type V isotherms, indicating the presence in mesopores [24]. This fact indicates that the presence of pores of as-dealloyed Ni<sub>30</sub>Al<sub>70</sub> alloy is larger than Ni<sub>50</sub>Al<sub>50</sub> alloy. In addition, the first layer energy constant of Brunauer-Emmett-Teller (BET) plot of as-dealloyed Ni<sub>50</sub>Al<sub>50</sub> alloy is negative due to the presence of micropores as shown in Fig. 8(b). BET surface area, pore volume and mean pore diameter for these as-dealloyed Ni<sub>30</sub>Al<sub>70</sub>, and Ni<sub>50</sub>Al<sub>50</sub> alloys are given in Table 1. The larger surface area is obtained in the np-Ni dealloyed from Ni<sub>30</sub>Al<sub>70</sub>, compared to that from Ni<sub>50</sub>Al<sub>50</sub>. This result is consistent with the microstructural observation shown in Fig. 5.

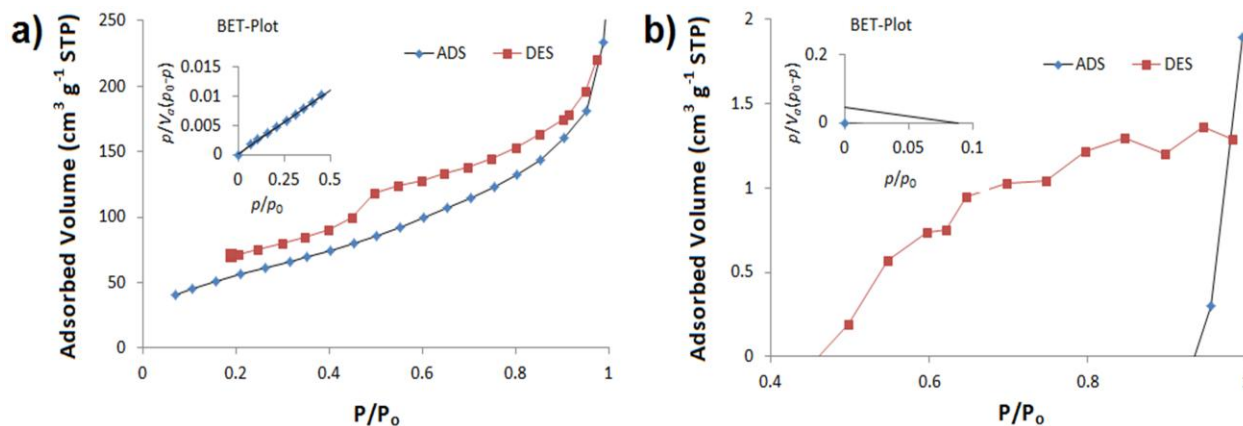


**Figure 8.** BET surface analysis and N<sub>2</sub> isotherms at -196 °C of porous Ni catalysts: a) Ni<sub>30</sub>Al<sub>70</sub> alloy, and b) Ni<sub>50</sub>Al<sub>50</sub> alloy dealloyed in 1 M NaOH at room temperature.

**Table 1.** Physicochemical characteristics of nanoporous Ni

Compositions of precursor alloy (at%)	BET surface area (S <sub>BET</sub> ) (m <sup>2</sup> g <sup>-1</sup> )	Pore volume (V <sub>pore</sub> ) (cm <sup>3</sup> g <sup>-1</sup> )	Mean pore diameter (d <sub>pore</sub> ) (nm)
Ni <sub>30</sub> Al <sub>70</sub>	198.68	3.655	74.71
Ni <sub>50</sub> Al <sub>50</sub>	-9.46	0.02	11.24

Fig. 9 shows the 3D profiles of surface roughness of the as-dealloyed np-Ni from Ni<sub>30</sub>Al<sub>70</sub>, and Ni<sub>50</sub>Al<sub>50</sub> alloys. As the surface roughness determines the micro-scale surface topography of a porous

material, thorough quantitative surface topography analysis is essential for modeling of porous structure [25]. There are three types of parameters for characterising surface topography: (i) the amplitude parameters, (ii) the spacing parameter, and (iii) the hybrid parameter. These three parameters can be determined with a 3D profiler that is coupled with *SurfVision* software. Amplitude parameters such as mean roughness ( $S_a$ ) and root mean square (RMS) roughness ( $S_q$ ) that measure the vertical characteristics of surface deviations have been used in this study and evaluated over the complete 3D surface. These parameters represent an overall description of the surface textures that enable the differentiation of peaks, valleys, and the spacing of surface textures [26]. In this study, the values of roughness amplitude parameters  $S_a$ , and  $S_q$  of dealloyed  $Ni_{30}Al_{70}$  alloy are  $1.147 \mu m$ , and  $1.611 \mu m$ , respectively, which are clearly greater than that of dealloyed  $Ni_{50}Al_{50}$  alloy of  $0.787 \mu m$ , and  $1.103 \mu m$ , respectively. The greater values of  $S_a$ , and  $S_q$  indicate that the surface is rougher of the porous structure which is similar to the SEM images shown in Fig. 5.

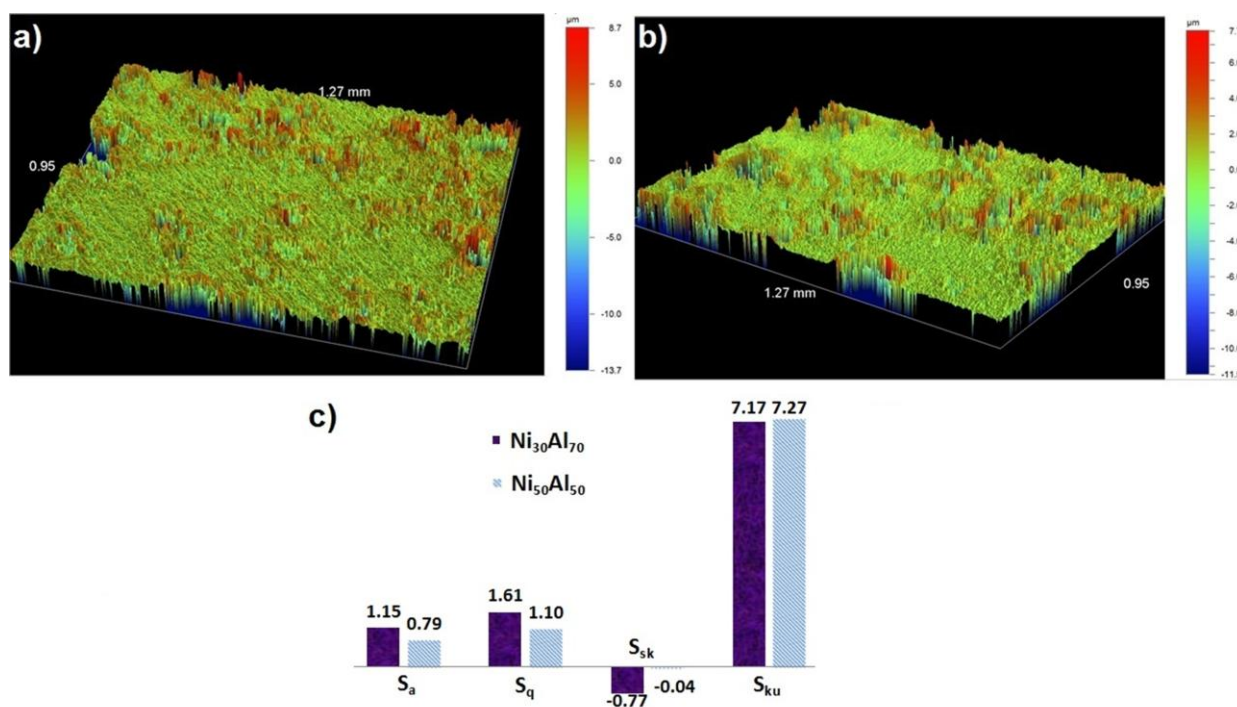


**Figure 9.** (a) 3D profile of porous surface of np-Ni dealloyed from  $Ni_{30}Al_{70}$ , (b) 3D profile of porous surface of np-Ni dealloyed from  $Ni_{50}Al_{50}$ ; and (c) comparison of the surface roughness parameters of the np-Ni dealloyed from  $Ni_{30}Al_{70}$ , and  $Ni_{50}Al_{50}$ .

In addition, the degree of symmetry of the surface heights about the mean plane is represented by  $S_{sk}$ , the skewness of a 3D surface texture, and it is the third central moment of the profile amplitude probability density function [26]. The sign of the  $S_{sk}$  indicates the most dominant nature of topography. For instance,  $S_{sk} > 0$  indicates high peaks; whereas  $S_{sk} < 0$  indicates deep scratches [26]. The more negative of  $S_{sk}$  values implies the more porous structure. In this study, we have found that the values of  $S_{sk}$  of the dealloyed  $Ni_{30}Al_{70}$  and  $Ni_{50}Al_{50}$  alloys are -0.767 and -0.039, respectively. This indicated that the dealloyed  $Ni_{30}Al_{70}$  was a more porous structure than dealloyed  $Ni_{50}Al_{50}$  alloy.

The nature of height distribution is indicated by Kurtosis ( $S_{ku}$ ) of a 3D surface texture which is the fourth central moment of profile amplitude probability density function and describes the sharpness of the probability of the profile [26]. For  $S_{ku} > 3.0$ , the distribution curve is leptokurtotic and indicating many high peaks and low valleys. In contrast, the distribution curve is platykurtotic at  $S_{ku} < 3.0$ , indicating relatively few high peaks and low valleys. In this study, the values of  $S_{ku}$  of dealloyed  $Ni_{30}Al_{70}$ , and  $Ni_{50}Al_{50}$  alloys are 7.174, and 7.273, respectively. Hence, it can be concluded that the two surfaces of the dealloyed np-Ni were leptokurtotic.

#### 4.2 Electrochemical performances of np-Ni as negative electrode of LIBs

Transition metal oxides are promising anode materials for high performance LIBs due to their large capacity ( $700 \text{ mA h g}^{-1}$ ) that based on the reaction mechanism given by:



where  $M = Fe, Co, Ni, Cu$  etc. The as-dealloyed np-Ni naturally forms an oxide (NiO) layer covering the inner-core when exposed to air and water, the core-shell Ni/NiO nanoporous structure dealloyed from  $Ni_{30}Al_{70}$  alloy was used as negative electrode of LIBs. During discharge, the NiO are reduced into highly dispersed metallic nanoparticles and  $Li_2O$ . During the subsequent charge, the  $Li_2O$  matrix decomposes and Ni nanoparticles converted back to NiO nanograins. Figure 10 shows galvanostatic discharge (Li intercalation)-charge (Li deintercalation) profiles of 1<sup>st</sup>, 9<sup>th</sup>, and 50<sup>th</sup> cycles at a current rate of 1C with the potential window of 1.5-4.2 V versus Li at room temperature. 1C means accomplishing discharge or charge in an hour.

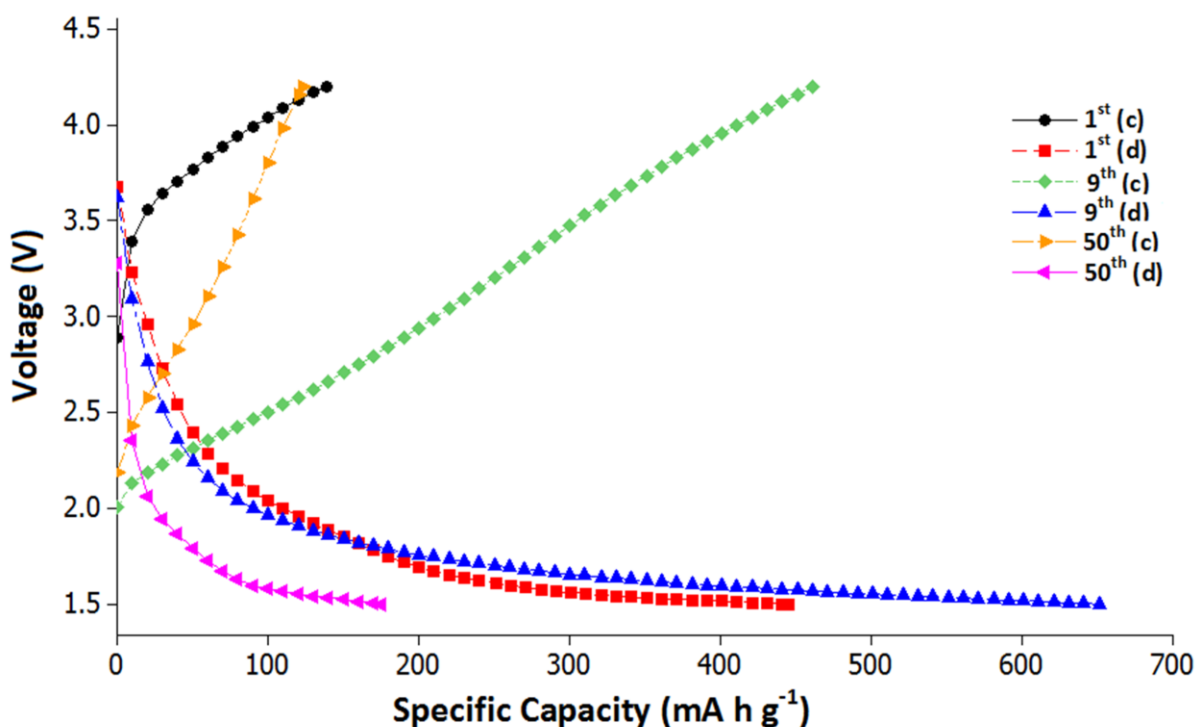


**Figure 10.** Representative charge and discharge voltage profiles at 1 C current rate.

It can be seen that the 1<sup>st</sup> discharge capacity is about 445 mA h g<sup>-1</sup>, much higher than the subsequent charge capacity of 139 mA h g<sup>-1</sup>. The irreversible capacity loss of 68.75% may be attributable to the formation of solid electrolyte interface (SEI). The formation of SEI is due to the electrochemically driven electrolyte degradation, and similar phenomenon was also observed in other systems operating through conversion reactions [27, 29, 30]. A reversible capacity of 499 mAh g<sup>-1</sup> was achieved in the 2<sup>nd</sup> cycle (Fig. 12) at a rate of 1C, which gradually increases to about 651 mAh g<sup>-1</sup> after 9<sup>th</sup> cycles, whereas the coulombic efficiency reached the values higher than 104%. The increasing specific capacity may be attributed to the reversible growth of a polymeric gel-like film resulting from the kinetically activated electrolyte degradation [31-34]. In addition, this electrochemical enhancement of nanoporous Ni/NiO as anode material might be attributable to the high surface area and high reactivity of the nanoporous structures. Thereafter, generally the reversible capacity decreased with cycling. The 50<sup>th</sup> reversible capacity reduced to 175 mA h g<sup>-1</sup> at 1C current rate, which showed 60.70 % of capacity fading to the 1<sup>st</sup> cycle. There is no possible plateau (conversion of NiO to Ni<sup>0</sup> and lithiation reaction to form Li<sub>2</sub>O) for discharge profile in the potential window of 1.5-4.2V. One possible reason is that the plateau forms in the potential window of 0.5-1.5V [30, 34-36].

To systematically investigate the electrochemical performance of nanoporous Ni/NiO electrodes, three consecutive cyclic voltammetry (CV) cycles are recorded at a scan rate of 0.1 mV s<sup>-1</sup> in the potential window of 0.02-4.20 V as shown in Fig. 11.

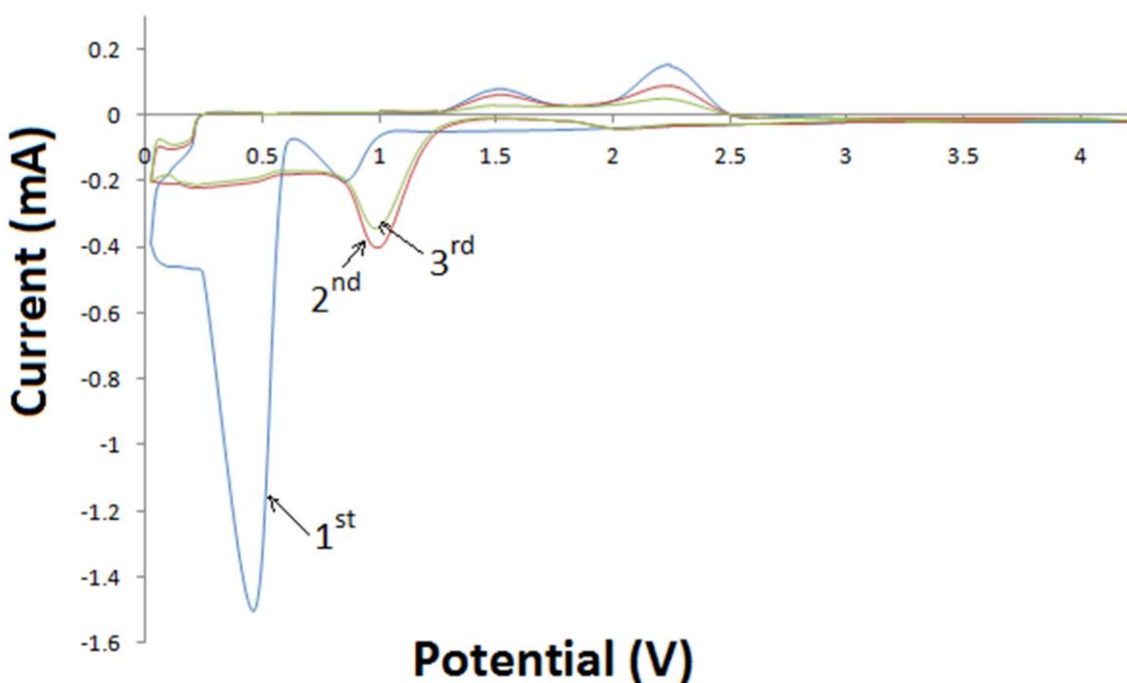


**Figure 11.** Cyclic voltammograms at a scan rate of 0.1 mV s<sup>-1</sup> of Ni/NiO electrodes.

In the first discharge cycle, two reduction peaks can be observed at 0.48 V and 0.78 V, respectively, corresponding to the initial reduction of NiO to Ni induced by a conversion reaction of

$\text{NiO} + 2\text{Li}^+ + 2\text{e}^- \rightarrow \text{Ni} + \text{Li}_2\text{O}$  and the decomposition of the electrolyte to form a partially reversible SEI layer [37]. However, there are two broad oxidation peaks in anodic process. The one at 2.25 V is due to the reversible oxidation of Ni to NiO by the chemical reaction  $\text{Ni} + \text{Li}_2\text{O} \rightarrow \text{NiO} + 2\text{Li}^+ + 2\text{e}^-$ , while the other one at 1.50 V due to the decomposition of SEI layer [35]. In the subsequent cycles, reduction peaks shift to about 1.05 V and 1.80 V, enduring oxidation peaks slightly shift to 2.22 V and 1.52 V. These two redox reactions of lithium ions with the nanoporous Ni/NiO electrodes are highly reversible.

The discharge capacity degraded in the subsequent cycles as shown in Fig. 12. The discharge capacity up to the 9<sup>th</sup> cycles was always close to the theoretical capacity ( $718 \text{ mAh g}^{-1}$ ) of NiO, due to the specific nanoporous structures of Ni/NiO and probably some unknown reactions of aluminum.

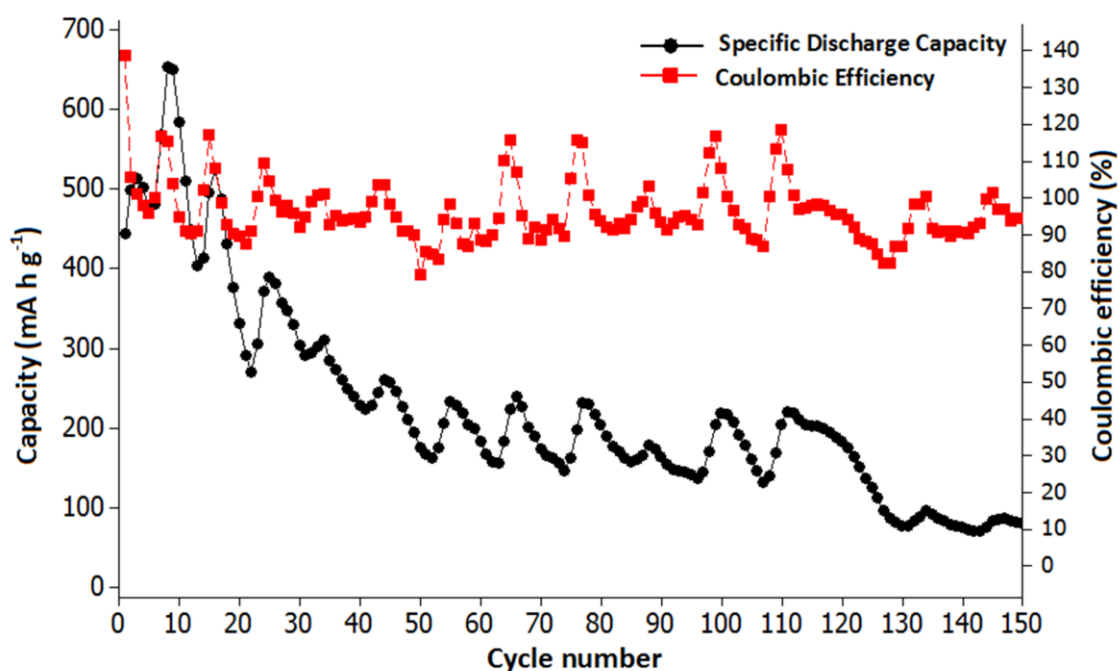


**Figure 12.** Cyclic performances of LIBs at a 1C current rate

The capacity fluctuated, and decreased to neglectable level of  $80 \text{ mAh g}^{-1}$  at 150<sup>th</sup> cycles. The severe capacity degradation and poor cycling performance is attributed to the large volume expansion/constriction leading to the pulverization and degradation of the nanoporous Ni/NiO electrode. The volume expansion/constriction also leads to the repeated destroy and formation of SEI film and accordingly the continuous consumption of the electrolyte [38]. The similar patterns trailed the coulombic efficiency of LIBs as shown in Fig.12. The 1<sup>st</sup> cycle coulombic efficiency of 139 % reduced to 94.7 % at 150<sup>th</sup> cycles. This fluctuation of the efficiency might be attributable as the formation of instable interfacial phenomenon, such as irregular formation and destruction of lithium dendrites, non-uniform surface passivation. However, the mean Coulombic efficiency of  $96.50 \pm 8.45$  is observed despite the high fluctuations of the efficiency from 1<sup>st</sup> to 150<sup>th</sup> cycles.

Figure 13 shows the Nyquist plot and equivalent circuit of nanoporous Ni/NiO fabricated from dealloying of Ni<sub>30</sub>Al<sub>70</sub> alloy in the frequency range between 100k to 10m Hz at room temperature. The Nyquist plot contains a high to medium frequency semicircle which is usually assigned to film resistance ( $R_f$ ) and film capacitance ( $C_f$ ) to the electrode surface films that is obviously cover all lithiated transition metal oxides in standard electrolyte solutions. In addition, the Nyquist plot of this nanoporous Ni/NiO electrode contains a medium to low frequency semicircle (inset of Fig. 13) that can be assigned to the interfacial charge-transfer resistance ( $R_{ct}$ ) and electric double-layer capacitance ( $C_{dl}$ ) coupled with the straight beeline in the low frequency region represents the typical Warburg impedance, which is related to the diffusion of lithium ions in the active Ni/NiO electrode. The impedance data were analyzed by using ZSimpWin software to suitable equivalent circuit as shown in inset of Fig. 13. After fitting the data, the values of electrolytes' resistance ( $R_s$ ),  $R_f$ , and  $R_{ct}$  are found to be 10.25  $\Omega$ , 12.80  $\Omega$ , and 5.50  $\Omega$ , respectively. In addition, the values of  $C_f$ ,  $C_{dl}$ , and  $W$  are found to be 63.20  $\mu\text{F cm}^{-2}$ , 1.45  $\mu\text{F cm}^{-2}$ , and 0.03 S. sec<sup>0.5</sup>, respectively. It is apparent that the charge transfer resistance of nanoporous Ni/NiO electrode is very small which can be attributed to the facile charge transfer at the nano-scale Ni/NiO walls-electrolyte interfaces. This reduced charge transfer resistance is benefit to enhance the electron kinetics in the electrode material. Hence, improve the electrochemical performances of nanoporous Ni/NiO electrode of lithium storage.

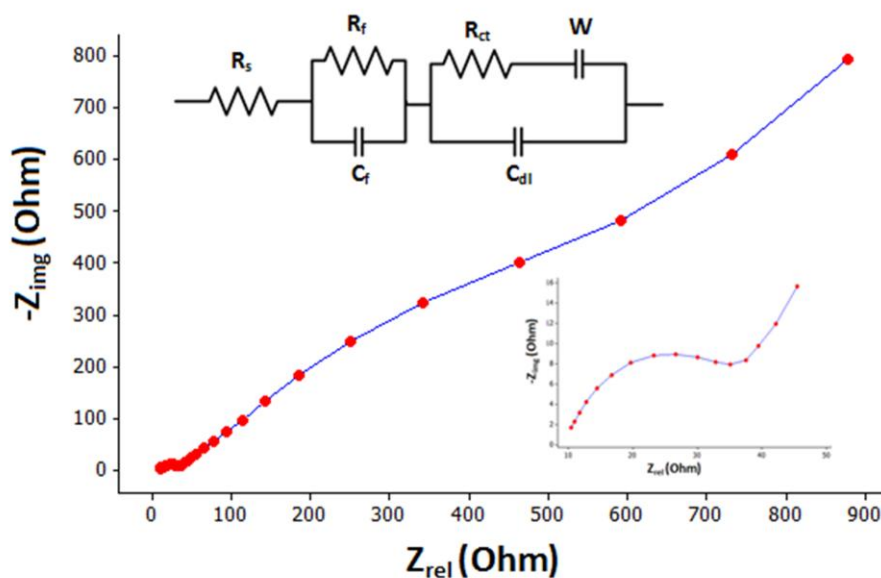


**Figure 13.** The Nyquist plot and equivalent circuit of nanoporous Ni/NiO fabricated from dealloying of Ni<sub>30</sub>Al<sub>70</sub> alloy in the frequency range between 100k to 10m Hz at room temperature (The inset is high to medium and medium to low frequency semicircles).

## 5. CONCLUSIONS

In this study, fabrication of np-Ni was attempted by dealloying the aluminum from Ni<sub>30</sub>Al<sub>70</sub> and Ni<sub>50</sub>Al<sub>50</sub> alloys. Alloy composition showed a significant effect on the microstructure and the

formation of the np-Ni. An inhomogeneous nanoporous structure was observed for the np-Ni dealloyed from Ni<sub>30</sub>Al<sub>70</sub>, whilst there were only a few pores at nanoscale observed in the dealloyed Ni<sub>50</sub>Al<sub>50</sub>. The np-Ni dealloyed from Ni<sub>30</sub>Al<sub>70</sub> exhibited a nickel oxide (NiO) layer on the surface. This nanoporous Ni/NiO core-shell structure was directly used as binder free electrodes for LIBs and the performance was assessed. The conclusions are as follows:

1. The np-Ni dealloyed from Ni<sub>30</sub>Al<sub>70</sub> and Ni<sub>50</sub>Al<sub>50</sub> exhibited a mean inner diameter of  $71.10 \pm 43.69$  nm and  $40.84 \pm 24.70$  nm, respectively. There was still residue aluminum remained in the np-Ni after dealloying since the metastable phases of Al<sub>3</sub>Ni<sub>2</sub> and Al<sub>3</sub>Ni in the Ni-Al alloys were difficult to dealloy.

2. The as-dealloyed np-Ni surfaces displayed a leptokurtotic roughness distribution. The specific surface area of the np-Ni dealloyed from Ni<sub>30</sub>Al<sub>70</sub> was  $198.70 \text{ m}^2 \text{ g}^{-1}$ ; while it was negative  $9.50 \text{ m}^2 \text{ g}^{-1}$  for the np-Ni dealloyed from Ni<sub>50</sub>Al<sub>50</sub>. The negative value of the specific surface area indicates that there were only a few pores presented in the np-Ni dealloyed from Ni<sub>50</sub>Al<sub>50</sub>.

3. The as-dealloyed np-Ni naturally formed and oxide (NiO) layer covering the inner-core (Ni) when exposed to air and water; the nanoporous Ni/NiO dealloyed from Ni<sub>30</sub>Al<sub>70</sub> alloy can be used as negative electrode of lithium ion batteries (LIBs).

4. The discharge capacity of the Ni/NiO with a nanoporous structure is  $651 \text{ mAh g}^{-1}$  at 1C rate after 9<sup>th</sup> cycle, which was decreased to a neglectable level of  $80 \text{ mAh g}^{-1}$  after 150<sup>th</sup> cycle. The unique nanoporous structure of Ni/NiO showed superior lithium storage performances at the initial charge-discharge cycles, although future research towards further improvement in cyclic stability is still needed.

#### ACKNOWLEDGEMENTS

This project is supported by the Australian Government through the Australia-India Strategic Research Fund (ST060048)

#### References

1. T. Gorbanyuk, A. Evtukh, V. Litovchenko, V. Solntsev, *Physica E* 38 (2007) 211.
2. A. Wittstock, J. Biener, M. Bäumer, *Phys. Chem. Chem. Phys.* 12 (2010) 12919.
3. M.F. Ashby, *Butterworth-Heinemann*, (2000).
4. J. Erlebacher, M.J. Aziz, A. Karma, N. Dimitrov, K. Sieradzki, *Nat.* 410 (2001) 450.
5. J. Erlebacher, R. Seshadri, *MRS Bulletin* 34 (2009) 561.
6. J. Zhang, C. M. Li, *Chem. Soc. Rev.* 41 (2012) 7016.
7. V. Zielasek, B. Jürgens, C. Schulz, J. Biener, M.M. Biener, A.V. Hamza, M. Bäumer, *Angew. Chem. Int. Ed.* 45 (2006) 8241.
8. L. Liu, E. Pippel, R. Scholz, U. Gösele, *Nano Lett.* 9 (2009) 4352.
9. X. Wang, W. Wang, Z. Qi, C. Zhao, H. Ji, Z. Zhang, *Electrochem. Commun.* 11 (2009) 1896.
10. B.C. Tappan, S.A. Steiner, E.P. Luther, *Angew. Chem. Int. Ed.* 49 (2010) 4544.
11. J. Baney, *US Patents 1628190A*, (1927).
12. O.B. Olurin, D.S. Wilkinson, G.C. Weatherly, V. Paserin, J. Shu, *Compos. Sci. Technol.* 63 (2003) 2317.
13. V. Paserin, S. Marcuson, J. Shu, D.S. Wilkinson, *Adv. Eng. Mater.* 6 (2004) 454.

14. C. Marozzi, A. Chialvo, *Electrochim. Acta* 45 (2000) 2111.
15. M.A. Rahman, X. Wang, C.Wen, *Proc. of ICMERE2013, Bangladesh*, (2013).
16. M. Vukmirovic, N. Dimitrov, K. Sieradzki, *J. Electrochem. Soc.* 149 (2002) B428.
17. A. Bradley, A. Taylor, *Proc. R. Soc. A* 159 (1937) 56.
18. Z. Qi, Z. Zhang, H. Jia, Y. Qu, G. Liu, X. Bian, *J. Alloys Compd.* 472 (2009) 71.
19. K. Sieradzki, R. Corderman, K. Shukla, R. Newman, *Philos. Mag. A* 59 (1989) 713.
20. H. Hu, M. Qiao, S. Wang, K. Fan, H. Li, B. Zong, X. Zhang, *J. Catal.* 221 (2004) 612.
21. P. Fouilloux, *Appl. Catal.* 8 (1983) 1.
22. M. Bartok, *Adv. Catal.* 36 (1989) 329.
23. J. Rouquerol, D. Avnir, C. Fairbridge, D. Everett, J. Haynes, N. Pernicone, J. Ramsay, K. Sing, K. Unger, *Pure Appl. Chem.* 66 (1994) 1739.
24. C. Sangwichien, G.L. Aranovich, M.D. Donohue, *Colloids Surf., A* 206 (2002) 313.
25. G. Kerckhofs, G. Pyka, M. Moesen, S. Van Bael, J. Schrooten, M. Wevers, *Adv. Eng. Mat.* 15 (2013) 153.
26. E.S. Gadelmawla, M.M. Koura, T.M.A. Maksoud, I.M. Elewa, H.H. Soliman, *J. Mater. Process. Technol.* 123 (2002) 133.
27. P. Poizot, S. Laruelle, S. Grugeon, L. Dupont, J. Tarascon, *Nat.* 407 (2000) 496.
28. S. Mitra, P. Poizot, A. Finke, J.M. Tarascon, *Adv. Funct. Mater.* 16 (2006) 2281.
29. X.W. Lou, D. Deng, J.Y. Lee, J. Feng, L.A. Archer, *Adv. Mater.* 20 (2008) 258.
30. S. Ni, T. Li, X. Lv, X. Yang, L. Zhang, *Electrochim. Acta* 91 (2013) 267.
31. S. Grugeon, S. Laruelle, L. Dupont, J.M. Tarascon, *Solid State Sci.* 5 (2003) 895.
32. L. Dupont, S. Laruelle, S. Grugeon, C. Dickinson, W. Zhou, J.M. Tarascon, *J. Power Sources* 175 (2008) 502.
33. G. Zhou, D.-W. Wang, F. Li, L. Zhang, N. Li, Z.S. Wu, L. Wen, G.Q. Lu, H.M. Cheng, *Chem. Mater.* 22 (2010) 5306.
34. X. Wang, X. Li, X. Sun, F. Li, Q. Liu, Q. Wang, D. He, *J. Mater. Chem.* 21 (2011) 3571.
35. H. Liu, G. Wang, J. Liu, S. Qiao, H. Ahn, *J. Mater. Chem.* 21 (2011) 3046.
36. L. Yuan, Z. Guo, K. Konstantinov, P. Munroe, H.K. Liu, *Electrochem. Solid-State Lett.* 9 (2006) A524.
37. S. Ni, T. Li, X. Lv, X. Yang, L. Zhang, *Electrochim. Acta* 91 (2013) 267.
38. L. Liu, Y. Li, S. Yuan, M. Ge, M. Ren, C. Sun, Z. Zhou, *J. Phys. Chem. C* 114 (2009) 251.

© 2015 The Authors. Published by ESG ([www.electrochemsci.org](http://www.electrochemsci.org)). This article is an open access article distributed under the terms and conditions of the Creative Commons Attribution license (<http://creativecommons.org/licenses/by/4.0/>).